

**Department of Physics and Astronomy**  
**University of Heidelberg**

Bachelor Thesis in Physics  
submitted by

**Robin Eberhard**  
born in Aalen, Germany

handed in on  
**March 28, 2016**

# **Characterization of a multispecies imaging system**

This Bachelor Thesis has been carried out by Robin Eberhard at the  
**Institute for Theoretical Physics in Heidelberg**  
under the supervision of  
**Prof. Dr. Matthias Weidemüller**

# Characterization of a multispecies imaging system

Robin Eberhard

**Abstract** Lorem ipsum dolor sit amet, consectetur adipiscing elit. Ut purus elit, vestibulum ut, placerat ac, adipiscing vitae, felis. Curabitur dictum gravida mauris. Nam arcu libero, nonummy eget, consectetur id, vulputate a, magna. Donec vehicula augue eu neque. Pellentesque habitant morbi tristique senectus et netus et malesuada fames ac turpis egestas. Mauris ut leo. Cras viverra metus rhoncus sem. Nulla et lectus vestibulum urna fringilla ultrices. Phasellus eu tellus sit amet tortor gravida placerat. Integer sapien est, iaculis in, pretium quis, viverra ac, nunc. Praesent eget sem vel leo ultrices bibendum. Aenean faucibus. Morbi dolor nulla, malesuada eu, pulvinar at, mollis ac, nulla. Curabitur auctor semper nulla. Donec varius orci eget risus. Duis nibh mi, congue eu, accumsan eleifend, sagittis quis, diam. Duis eget orci sit amet orci dignissim rutrum.

**Zusammenfassung** Lorem ipsum dolor sit amet, consectetur adipiscing elit. Ut purus elit, vestibulum ut, placerat ac, adipiscing vitae, felis. Curabitur dictum gravida mauris. Nam arcu libero, nonummy eget, consectetur id, vulputate a, magna. Donec vehicula augue eu neque. Pellentesque habitant morbi tristique senectus et netus et malesuada fames ac turpis egestas. Mauris ut leo. Cras viverra metus rhoncus sem. Nulla et lectus vestibulum urna fringilla ultrices. Phasellus eu tellus sit amet tortor gravida placerat. Integer sapien est, iaculis in, pretium quis, viverra ac, nunc. Praesent eget sem vel leo ultrices bibendum. Aenean faucibus. Morbi dolor nulla, malesuada eu, pulvinar at, mollis ac, nulla. Curabitur auctor semper nulla. Donec varius orci eget risus. Duis nibh mi, congue eu, accumsan eleifend, sagittis quis, diam. Duis eget orci sit amet orci dignissim rutrum.

# Contents

<b>1. Introduction</b>	<b>1</b>
<b>2. Setup for high resolution imaging</b>	<b>2</b>
2.1. Experimental requirements . . . . .	2
2.1.1. Experimental setup . . . . .	2
2.1.2. Basics of CCD cameras . . . . .	3
2.2. Camera for double species imaging . . . . .	4
2.2.1. Comparison with the present setup . . . . .	4
2.2.2. Dark current . . . . .	5
2.2.3. Readout noise . . . . .	6
2.2.4. Quantum efficiency . . . . .	8
2.2.5. Pixel correlations . . . . .	8
2.3. Mechanical shutter . . . . .	9
2.3.1. Electronic and mechanical setup . . . . .	9
2.3.2. Dynamical properties . . . . .	10
2.4. Mask for the CCD sensor . . . . .	13
2.4.1. Fast kinetics mode . . . . .	13
2.4.2. Frequency response of a slit . . . . .	15
2.4.3. Optimization of the masking setup . . . . .	19
<b>3. Testing the camera: Superfluids</b>	<b>20</b>
3.0.1. Absorption imaging . . . . .	20
3.1. Previous observations in a polarized fermi gas . . . . .	21
3.2. Implementation in the setup . . . . .	22
<b>4. Conclusion and outlook</b>	<b>24</b>
<b>A. Acquisition sequence</b>	<b>25</b>
<b>B. Shutter circuit</b>	<b>27</b>

<b>C. Setup of the custom slit</b>	<b>29</b>
------------------------------------	-----------

# 1. Introduction

- Nothing yet...

## 2. Setup for high resolution imaging

### 2.1. Experimental requirements

#### 2.1.1. Experimental setup

In the experiment, atoms are trapped and cooled inside a vacuum chamber. The setup [1] consists of a double species mixture, Lithium and Caesium, which are focused into the centre of the chamber, where they can be confined using at first a magneto-optical trap (MOT). The atoms are cooled using doppler cooling, where six laser beams are set up to cross each other in the centre. They act as a net force on atoms moving against the propagation direction of the beam, so that fast atoms are slowed down, but slow atoms are not sped up. Atoms are trapped at the same time, using magnetic coils in anti-helmholtz configuration. The magnetic field will therefore be strong on the bounds of the trap and zero in the center, so that atoms that are off-center receive a higher force.

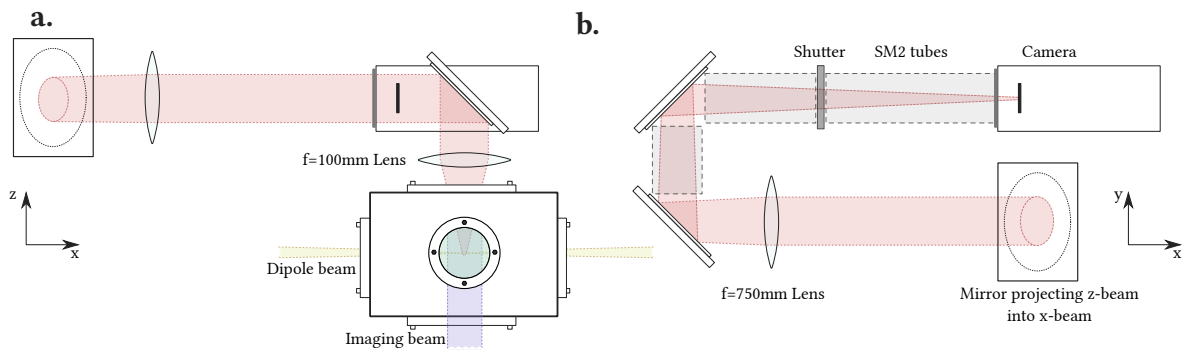


Figure 2.1.: **Imaging path.** The camera is mounted above the vacuum chamber as visible in **a.** (gravity would be in negative  $z$  direction). The image of the atoms is collimated with the first lens and passing the optics in **b.**, until it is refocused in the chip on the camera.

In a next step, the atoms are transferred into an optical dipole trap, where they are further cooled evaporatively by only selecting the slowest atoms. A biconvex lens focuses the

imaging beam onto the CCD camera, which is located on top of the vacuum chamber. To minimize the incident background light, the imaging path is covered in SM2 tubes, which can be directly connected to the camera.

As the camera is also very sensitive to stray light, it has to be protected between measurements with a shutter, that covers the front end of the imaging path, such that no light will enter the camera, which is described in more detail in Section 2.3

### 2.1.2. Basics of CCD cameras

A camera operates by means of converting photons first into electrons then into voltage, which is finally read out as data [2] [3]. Each conversion process can add noise to the final image, which needs to be minimized in order to acquire accurate data. The most common noise sources are covered in Chapter 2.2.

The photons are collected on an array of semiconductor photo diodes, called the pixels, where ideally the spacing between the pixels is zero to gain maximum accuracy. The resolution is then dependent on the pixel size, which is for scientific cameras usually between  $10\text{ }\mu\text{m}$  and  $20\text{ }\mu\text{m}$  per pixel. Bigger pixels means higher photon sensitivity but usually lower resolution.

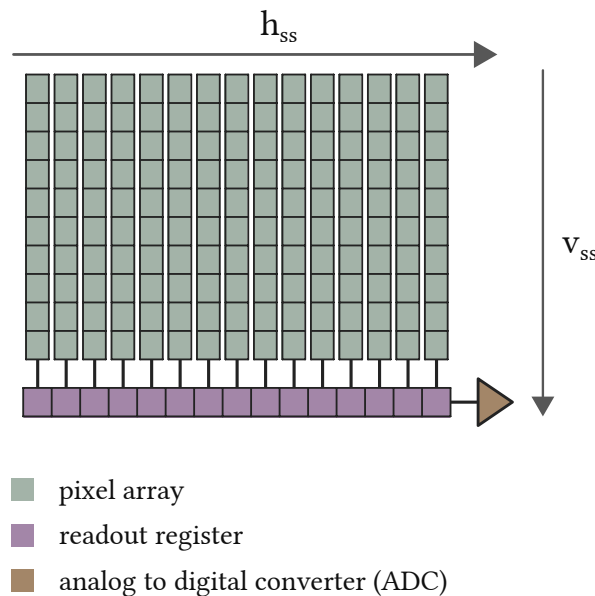


Figure 2.2.: **Schematic design of a CCD array and its readout.** The pixels are arranged in the pixel array. During readout they are shifted into the readout register and then to the side into the analog to digital converter



To create a digital image, the charge from the pixels have to be shifted one-by-one into the analog digital converter (ADC). This is done, by vertically shifting them into the readout register and then horizontal into the ADC, where the charges are multiplied and converted to digital data.

The shifting is done by storing the charges after collecting them, where each storage can be seen as an electronic potential well. In order to shift the charges and prevent overlapping, three spatially separated regions with potentials  $U_1$ ,  $U_2$  and  $U_3$  are required. Figure 2.3 indicates the systematics behind the shifting.

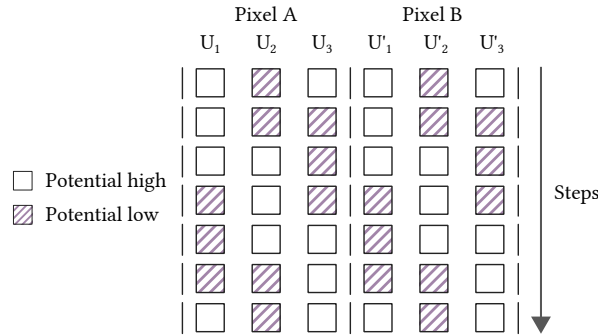


Figure 2.3.: **Shifting charges in a CCD detector.** To shift charges from Pixel A to Pixel B, the three potentials at the regions  $U_1$ ,  $U_2$  and  $U_3$  in each pixel have to be set accordingly to allow the charge flow without overlapping each other. Each row represents a single step.

Moving electrons to the next region is a three-step process. The charges are first only present in the region  $U_2$ , while the potentials  $U_1$  and  $U_3$  are kept high. They are then distributed across  $U_2$  and  $U_3$  by setting them both low. At last  $U_2$  will be set high such that the charge is now fully in  $U_3$ . This is repeated until the charge has been finally shifted from pixel A to B, which in total takes seven steps.

## 2.2. Camera for double species imaging

### 2.2.1. Comparison with the present setup

For the imaging of small atomic clouds, it is very important to have cameras with optimal noise and maximal readout speed. The new setup improves on both attributes. The dark noise can be significantly reduced by cooling the chip down to more than 70 °C. A new readout mode, called fast kinetics, makes it possible to acquire all images before reading out. This significantly improves the speed at which images can be taken.

The readout speed is highly important in our setup. Since absorption imaging is the technique of choice to measure atom attributes, three images need to be taken each sequence, being the absorption, division and background image. The old setup used a Guppy-38B [4] camera, which has a frame rate of 30fps. This meant the acquisition was finished after 100 ms. The Andor camera, on the other hand, can take images quickly without the need to read out in-between. At the fastest shift speed, the acquisition is finished after 1.632 ms, improving the speed by a factor of more than 60.

The quantum efficiency is explained in Chapter 2.2.4 and is also highly important, as it describes how many photons are detected on a camera and is directly connected to the sensitivity. A higher quantum efficiency therefore means better results.

When comparing the resolution, the chip size also has to be considered. Since higher resolutions seem to be preferable at first, it also means that for the same pixel sizes, the photon sensitivities will decrease. The pixel sizes compare to  $8.4\mu\text{m} * 9.8\mu\text{m}$  to  $13\mu\text{m} * 13\mu\text{m}$  from the old versus the new setup respectively, while the resolutions are  $768 \times 492$  and  $1024 \times 1024$  making a larger magnification now possible.

The Guppy camera is a lot smaller than the Andor iKon M ( $48.2\text{ mm} \times 30\text{ mm} \times 30\text{ mm}$  vs  $204.2\text{ mm} \times 105\text{ mm} \times 107\text{ mm}$ ), therefore making an implementation on a full experimental table easier. To implement such a complicated camera system that the Andor is, a lot of preparation was made in the thesis of Carmen Renner [5].

Nevertheless, despite its size, the new camera offers the ability to image both Lithium and Caesium species at once, while two Guppy cameras were needed beforehand, which also meant placing them on different imaging axes.

### 2.2.2. Dark current

A common noise source that is apparent in all CCD cameras, is the so-called dark current [6] [7]. It originates from the thermal excitation of electrons in individual pixels. Since they are made of semiconductors, once in a while, an electron can pass the potential between valence and conduction band simply due to their thermal energy. Thus, excess electrons accumulate, that contributes to the background signal and introduces additional noise.

The dark current has a strong temperature dependence

$$I_{\text{dark}}(T) \propto T^{\frac{3}{2}} \exp(-E_g/2k_B T), \quad (2.1)$$

QE of  
guppy?

look up  
qe of  
andor

would  
be great  
to have  
maybe  
an im-  
age  
of the  
atoms  
with  
the old  
and  
new  
setup  
(maybe  
same  
cooling  
steps  
etc.)

while  $E_g$  is the band gap, that separates the valence from the conduction band in the semiconductor,  $T$  the temperature and  $k_B$  the Boltzmann constant. Therefore in order to reduce dark current noise, the temperature of the chip can be reduced, which decreases the thermal energy of the electrons.

This has been measured and verified in Figure 2.4, using the built-in peltier element in the Andor camera to control the temperature of the CCD chip. For a long exposure time, dark current accumulates on all pixels. The counts are measured for several temperature settings and the counts  $C$  are converted to electrons per pixel per second ( $I_i$ ) [6] for each pixel  $i$  as

$$I_i = \frac{C}{Gt_{exp}} \quad (2.2)$$

with the Gain  $G$  of the camera, and the exposure time  $t_{exp}$ . The readout time of the pixels can be neglected, as they are significantly lower than the exposure time (see Chapter 2.4.1). The data should then follow the theory in Equation 2.1, although deviations are visible in the low temperature regime, which result from the fan not being able to divert the heat from the chip.

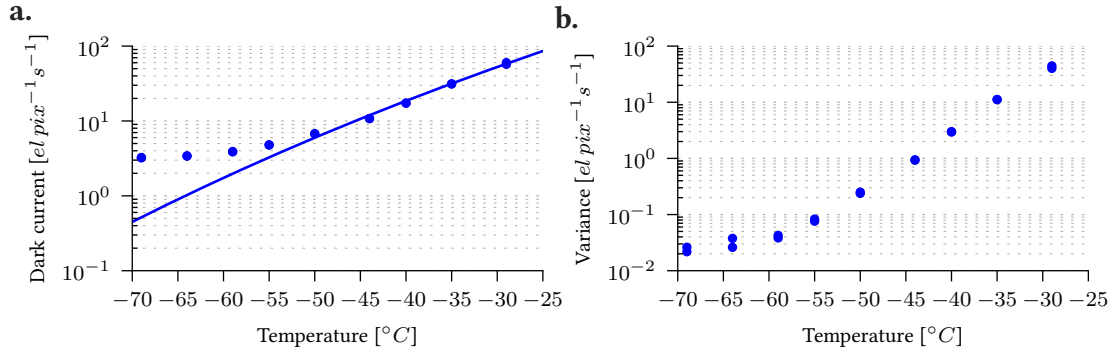


Figure 2.4.: **Dark noise accumulation on the chip.** For a long exposure time of 100 s, the dark current was measured for several temperatures. Gain in this measurement was minimal (0.215 [5]). Equation 2.1 was fitted, leaving the amplitude  $A$  and band gap  $E_g$  free, which resulted in  $A = 1.1 \cdot 10^8\ Wm^{-1}\ K^{-1}$  and  $E_g = 0.96\ eV$ .

### 2.2.3. Readout noise

As described in Chapter 2.1.2, pixels are shifted in order to be read out by the ADC. Moving charges from pixel to pixel causes noise that accumulates over each iteration. Together with the noise which the ADC introduces, this is then called the readout noise. The shifting noise

together with the dark noise is visible as a gradient () since each shift adds new charges due to excitations in the semiconductors. In order to characterize this, one can take the variance of the image, which should be zero for no noise.

figure  
with  
shift  
gradi-  
ent

In Figure 2.5 it has been shown, that slow readout speeds reduces the noise, although the vertical shift speeds do not seem to influence the noise at all. The measurement was carried out by taking images at low exposure time and low temperature, so that the main noise source would be the readout and not the dark current. Therefore the variance in the plot shows the noise from readout which goes to zero as the horizontal speed is decreased.

Shifting charges means increasing and decreasing potential wells, so that they can move from one into the other. If this is done fast enough (non-adiabatic), electrons in the pixel are more likely to get excited from the valence to the conduction band from the semiconductor, therefore adding noise. As a result from this, slower readout speeds are used in order to not add significantly more noise.

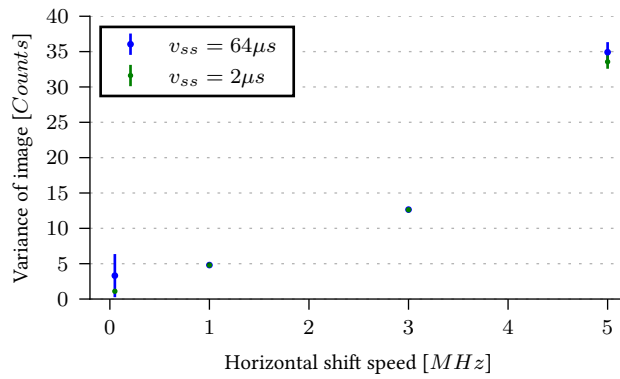


Figure 2.5.: **Readout noise.** The pixels are shifted row-wise into the readout register, depending on the vertical shift speed ( $v_{ss}$ ) and then moved pixel-by-pixel with the horizontal shift speed into the analog to digital converter. Since noise reduction is important, minimal horizontal shift speeds will be used, while the vertical shift speed does not seem to affect the variance. To make the readout the dominant noise source, temperature was set to  $-69^\circ\text{C}$  and exposure to 10 ms. The results have been received from taking the mean and variance of multiple sets of exposures.

### 2.2.4. Quantum efficiency

When selecting cameras for scientific imaging, one of the attributes to look out for is quantum efficiency (QE). Not all incoming photons are converted into electrons, which adds an uncertainty and additional noise to measurements. This is characterized by quantum efficiency, which is defined as the fraction of photons that are converted into electrons. A QE of 100% would mean, that every incident photon is converted into an electron on the chip. This can be put into equations as

$$QE = \frac{N_{detected}}{N_{total}}, \quad (2.3)$$

where  $N_{detected}$  describes the number of detected photons and  $N_{total}$  the number of photons that were sent from the laser beam.

The measurement of the quantum efficiency has been previously carried out by Carmen Renner [5] in her diploma thesis. In order to do that, the detected photons can be rewritten according to [8]:

$$N_{total} = \frac{E_{beam}}{E_{\gamma}} = \frac{Pt_{exp}}{E_{\gamma}} \quad (2.4)$$

where the energy of all photons reaching the camera  $E_{beam}$  is described with the power  $P$  and exposure time  $t_{exp}$ . The photon energy  $E_{\gamma}$  is calculated from  $E_{\gamma} = h\nu$ .

Now the quantum efficiency reads as

$$QE = \frac{h\nu N_{detected}}{Pt_{exp}}. \quad (2.5)$$

In order to find the QE, one would now measure the accumulated counts for several exposure times, since the frequency  $\nu$  and the power  $P$  are known. For the Andor camera used in our experiment, they have been measured as 70.7 % for 671 nm and 69.9 % for 852 nm.

This camera was especially chosen from the quantum efficiency, since it is important in our case, to be able to detect most photons from Lithium and Caesium absorption.

### 2.2.5. Pixel correlations

- Mainly the measurement (TBD)
- Some example images here maybe?

## 2.3. Mechanical shutter

### 2.3.1. Electronic and mechanical setup

The high QE of the Andor camera translates into a high sensitivity of the CCD chip to stray light. Therefore, in order to not unnecessarily illuminate the chip between measurements, a mechanical shutter was built into the optical path, which can also be seen in Figure 2.1. By opening the shutter shortly before the imaging sequence and closing it immediately afterwards, the stray light that is implying the CCD detector can be minimized.

cite  
andor  
manual  
some-  
where

The shutter has five fans, as seen in , which are mechanically guided, such that they together perform a circular motion outwards. The circular motion is best achieved for narrow fans, therefore needing more in order to close the shutter properly.

appendix  
image

The guides are connected to each other and can be pulled outwards with a mechanical switch, that can be manually pushed or pulled. To drive the shutter electronically, a magnetic coil and a magnet are used. When the coil receives a current, the magnet, which is connected to the switch will pull the guides, moving them outwards, therefore opening the shutter.

Although the coil can pull the magnet in, it cannot be pushed away. This is compensated using a spring, which is connected to the switch. This also means, that the current driving the coil needs to be high enough, to also work against the spring.

The most optimal case would be now to have fast opening and closing times, since again we want to prevent illumination between measurements. This can be achieved by testing several springs and to make the pull from the magnetic coils as fast as possible, which means increasing the current to drive it.

A custom circuit as outlined in Figure 2.6 is used. In order to serve a high current to increase the pull from the magnetic coil on the magnet, a transistor is used which is controlled by a MOSFET driver. The complete circuit also contains a voltage regulator, so that the user does not need to know the input of the driver and can simply serve a high voltage to open the shutter ( $V \in [2, 8]$  V) and a low voltage ( $V = 0$  V) to close it.

verify  
current  
678

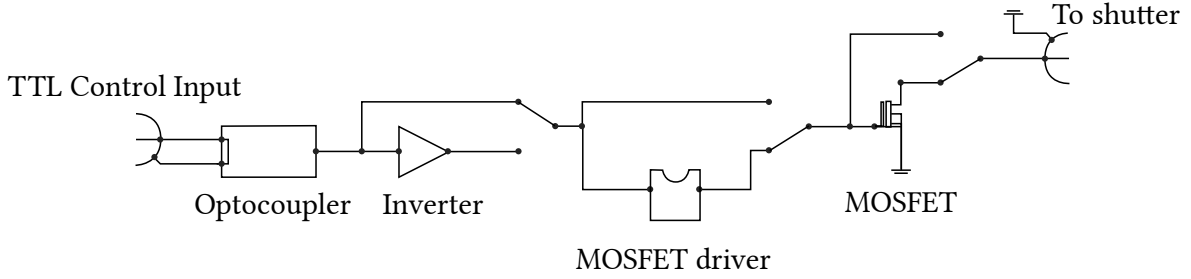


Figure 2.6.: **Electronic circuit to control the shutter.** The first element in the circuit is the optocoupler which is used to decouple parts from the circuit in order to not create loops, which would induce charges when the magnetic fields are on. The remaining parts can be skipped, by setting the jumpers. The inverter will flip the sign on the voltage. The MOSFET driver is used in order to serve the correct voltage at the transistor's gate and to help during discharge, such that the MOSFET will not overheat. The transistor will finally serve a high current of 2.5 A, that is throughput to the shutter. The jumpers in this figure are set as they are used in the experiment. The complete circuit can be found in Appendix B.

### 2.3.2. Dynamical properties

The shutter operates by controlling a magnetic coil, which pulls a magnet. The magnet is reverted into its original position by a spring, closing the shutter. It was discussed before, in Subsection 2.3.1, that more fans give a better approximation to a circular motion. Optimally, we would expect the shutter to open perfectly circular with linear velocity. Therefore, to optimize on this, one would look at opening and closing speeds, which should be minimal.

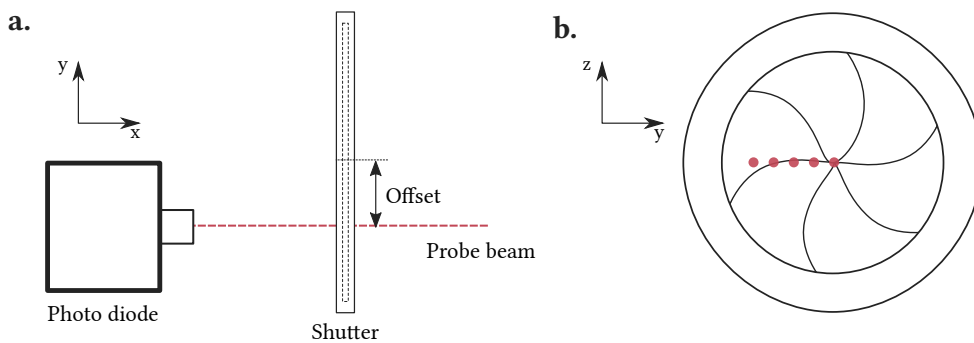


Figure 2.7.: **Probing the shutter for dynamics.** The shutter is probed at several positions using a laser. The offset in  $y$  direction was varied to find opening and closing times as a function of their offset.

To find the actual dynamics of the shutter, an experiment was set up. The shutter was probed at several positions, using a laser, to find the opening time. An example of one

of many measurements is shown in Figure 2.8. The laser beam has a gaussian intensity distribution, which results in a error function on the photodiode.

The points have been found by pointing a laser beam at a photodiode, which was blocked by the shutter. Since the laser has a finite radius, there is a transition in the signal from the minimum to the maximum, which is due to the approximately linear opening velocity of the shutter and the gaussian intensity distribution of the laser beam.

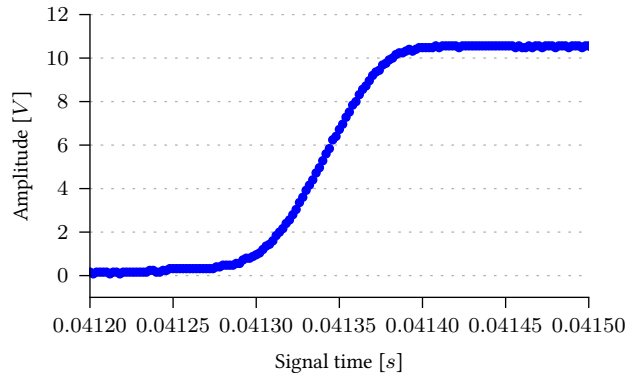


Figure 2.8.: **Shutter characterization.** The dynamics of the shutter were measured using a laser with a variable horizontal offset, which is fixed in this plot, and a photodiode measuring the laser intensity. In this figure, the offset is 9.3 mm from the center. An error function was fitted yielding the time until the shutter opens. The opening time was hereby defined, where the error function has its mean value, in this example being 5.2 s.

In order to find the opening and closing times of the shutter as seen in Figure 2.9a., the offset from the center of the laser to the shutter centre was varied. For larger offsets, the time from the initial trigger until a signal in the photodiode was received takes longer when the shutter is opening, while it takes shorter when it is closing. In Figure 2.9b. the speed is not perfectly linear. The deviations close to the centre originate from the shape of the fans. As there are five fans, there is no mirror symmetry, so that opening to the left and right is different in the end.

These measurements will later be used to time the triggers in the measurement, so that the shutter can stay closed as long as possible. But in order to optimize it, there were two shutters at hand, and several springs to choose from, the combination of which were all tested until the timings for opening  $t_{open} = 0.12$  and for closing  $t_{closing} = 0.14$  were found.



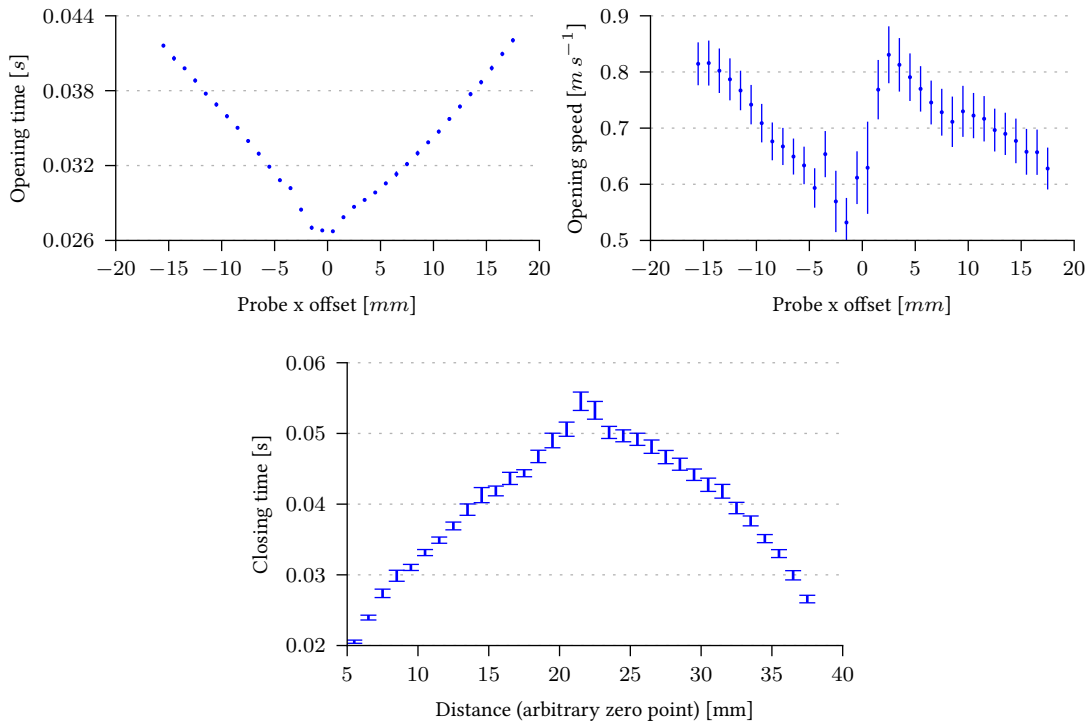


Figure 2.9.: **Sample dynamics.** The figure shows opening and closing time as well as the opening velocity for a strong spring. The spring closed the shutter quickly while it prevented it from opening fast. The velocity was measured by using the beam diameter as the distance the shutter needed to transverse. For each offset, a set of 100 images were taken and the errors found as being the variance. It is noticeable, that the opening velocity on the right side is faster at first than on the left side. This is due to the structure of the shutter, as can be seen in [Appendix image of shutter]. The overall opening speed on the other hand is not affected by this and seems to be linear with the offset.

It has been found that the opening time consists of actually three timings. The initial trigger signal runs through the electronics, until it is sent to the shutter coil. The coil then has a delay, until it starts pulling the magnet. The opening time is then found by also adding the time until the fans are fully open. This is also shown in Figure 2.10.

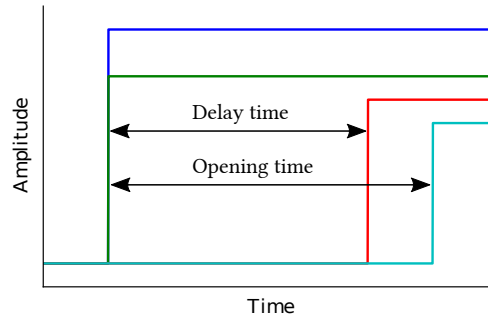


Figure 2.10.: **Shutter opening timings.** In the figure, the four signals show the timings until the shutter is open. The blue signal is the trigger that is sent from the user to start the opening sequence. The electronics add some minor delay, which is about a few nanoseconds until they send out the green trigger. After a certain delay time, which is most likely due to the coil needing to accumulate charge first, the red signal indicates when the shutter starts to open at the centre. The opening sequence is finished, when the shutter is fully open, which is shown by the turquoise line.

## 2.4. Mask for the CCD sensor

### 2.4.1. Fast kinetics mode

The fast kinetics mode allows the image acquisition to be only dependant on the vertical shift speed, reducing the acquisition time significantly. In this mode, only a portion of the CCD is illuminated, while the dark parts of the chip will be used as a storage. This means, that as soon as an image is taken, the illuminated pixels are shifted vertically behind a mask, such that no photons can reach them any more. When the chip is full or the user has finished their acquisition, the readout process is started.

As explained earlier in Chapter 2.1.2, the readout consists of first shifting a row into the readout register and then horizontally shifting them into the ADC. This is a very time consuming process, since the total readout time is described by

$$t_{ij} = i * v_{ss} + (i - 1) * j_{max} * h_{ss} + j * h_{ss}, \quad (2.6)$$

where  $v_{ss}$  and  $h_{ss}$  indicate the vertical and horizontal shift speed respectively. With this equation, the readout time until a pixel with the coordinates  $i$  and  $j$  is shifted into the readout register can be calculated. The readout of all pixels beforehand is also taken into account by  $j_{max}$  which is the width of the chip in pixels (1024 for the iKon M camera).

As can be seen, in the terms of the horizontal speed, the position of the last pixel in a row has a quadratic dependency. This is the dominant contribution to the readout time, which is necessary to shift the pixels into the ADC. At this point, the speed should not matter too much any more, because the experiment is already finished and the pixels are not illuminated any more.

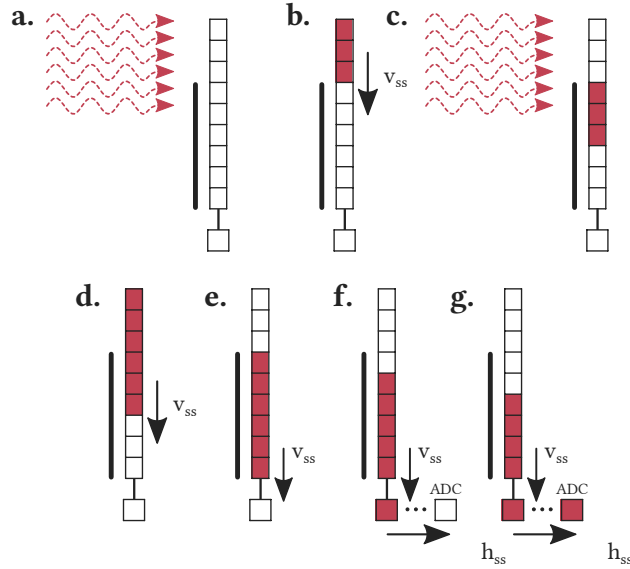


Figure 2.11.: **Schematics of imaging in the fast kinetics mode.** **a.** Laser photons excite electrons in pixels, creating the first absorption image. **b.** The illuminated pixels are shifted down behind a cover, while the laser is shut off. **c.** The second absorption image is taken without affecting the last measurement. **d.** Both images are shifted down before starting the readout process, to not falsify the data with stray light. **e.** The readout process starts, the first row is shifted into the readout register. **f./g.** The first pixels are shifted into the ADC. It is repeated until the complete chip has been read out.

To set up the fast kinetics mode, there are several parameters that need to be set in advance.

- **Series length.** The number of images acquired before the readout phase is initiated.
- **Exposed rows.** The height of an image in the fast kinetic series.
- **Offset from bottom.** Number of rows from the bottom of the chip, which are used as a temporary storage for the illuminated pixels.

It can be easily seen that the parameters are limited by the height of the CCD in pixels:

$$\text{Exposed rows} + \text{Offset from bottom} \leq 1024 \text{ px} \quad (2.7)$$

and

$$\text{Series length} * \text{Exposed rows} \leq \text{Offset from bottom.} \quad (2.8)$$

Therefore, in our application, we chose to exposure 204 px with an offset of 820 px, which gives a series length of 4. The pixels that are used as temporary storage of accumulated charge until the readout process begins need to be shielded from light. This is achieved with a slit in the front of the camera that blocks part of the light beam imaging the CCD detector.

Since we will be imaging two species, an absorption image for each species will be followed by two division images.

### 2.4.2. Frequency response of a slit

The slit is an optical element in the path, which will introduce diffraction on the chip – an effect due to the wave nature of light. Figure 2.12 sketches the systematics behind a laser wave approaching a slit.

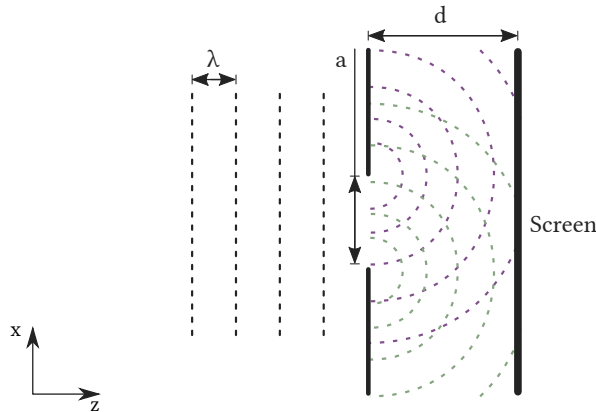


Figure 2.12.: **Diffraction on a single slit.** A planar wave with the wavelength  $\lambda$  approaches a slit with a width  $a$ , where the maxima of the wave are drawn as dashed lines. After the slit, Huygens principle is sketched as spherical waves, (purple and green), interfering with each other. The new wavefront is created where the waves cross each other and is as such visible on the screen to the right.

The incoming planar wave can be described by the formula:

$$E(x, z) = E_0 e^{-ikz}, \quad (2.9)$$

where the wave is propagating in the  $z$ -direction with the wave number  $k$  and an amplitude  $E_0$ .

It is known from Huygens principle, that each point from a planar wave can be seen as the origin of a spherical wave. The spherical waves will interfere with each other and because of the superposition principle a new wavefront will be built up.

The mathematical formalism of Huygens principle is simply the sum of all spherical waves, which for infinitely small distances is given as [9]:

$$E(x, z) = E_0 C \int_{Slit} \frac{1}{r^2} \exp(-ikr) dx'. \quad (2.10)$$

Here,  $r = \sqrt{(x - x')^2 + z^2}$  is the radius of a two dimensional wave,  $C$  is a normalization constant. Taylor expansion of the radius for  $z$  allows us, to substitute  $r^2$  with  $z^2$  and  $r$  with  $\frac{(x-x')^2}{2z} + z$ , while also the approximation  $(x - x') \ll z$  needs to be fulfilled. Therefore we get:

$$E(x, z) = E_0 e^{-ikz} \sqrt{\frac{ik}{2\pi z}} \int_{Slit} \exp\left(-\frac{ik}{2z}(x - x')^2\right) dx'. \quad (2.11)$$

The normalization was derived from the gaussian normal distribution  $\exp(-\frac{ik}{2z}(x - x')^2)$ . The integral will run over the slit size, with the origin in its middle and width  $a$ . We want to also write the exponential as a function of  $-\frac{i\pi t^2}{2}$ , due to the definition of fresnel integrals. The substitution follows:

$$\frac{k}{2z}(x - x')^2 = \frac{\pi t^2}{2}, \quad (2.12)$$

$$\Rightarrow t = \sqrt{\frac{k}{z\pi}}(x - x'), \quad (2.13)$$

$$\Rightarrow dx' = -dt \sqrt{\frac{z\pi}{k}}, \quad (2.14)$$

such that the field becomes

$$E(x, z) = -E_0 e^{-ikz} \sqrt{\frac{i}{2}} \int_{t(-a/2)}^{t(a/2)} \exp\left(-\frac{i\pi t^2}{2}\right) dt. \quad (2.15)$$

The fresnel integrals are defined by

$$C(x) = \int_0^x \cos\left(\frac{\pi t^2}{2}\right) dt, \quad (2.16)$$

$$S(x) = \int_0^x \sin\left(\frac{\pi t^2}{2}\right) dt, \quad (2.17)$$

so that in combination with Eulers equations and splitting up the integrals the equation for the electric field is:

$$E(x, z) = E_0 \sqrt{\frac{i}{2}} e^{-ikz} [C(-a/2) - C(a/2) - iS(-a/2) + iS(a/2)]. \quad (2.18)$$

In a real experiment, the light on a CCD chip is detected as intensity, which is given by

$$I(x, z) = \frac{2|E(x, z)|^2}{\epsilon_0 c}, \quad (2.19)$$

with the dielectric constant  $\epsilon_0$  and the speed of light  $c$ .

To verify the theory, we set up a simple experiment with a collimated laser beam pointing at the CCD of the Andor camera, with a slit in between. Such behaviour was also observed in our measurements. Figure 2.13 shows the diffraction pattern that was recorded with the Andor camera and a slit. A large, collimated beam was used to illuminate a slit in front of the CCD detector. Well resolved interference fringes can be observed by the slit.

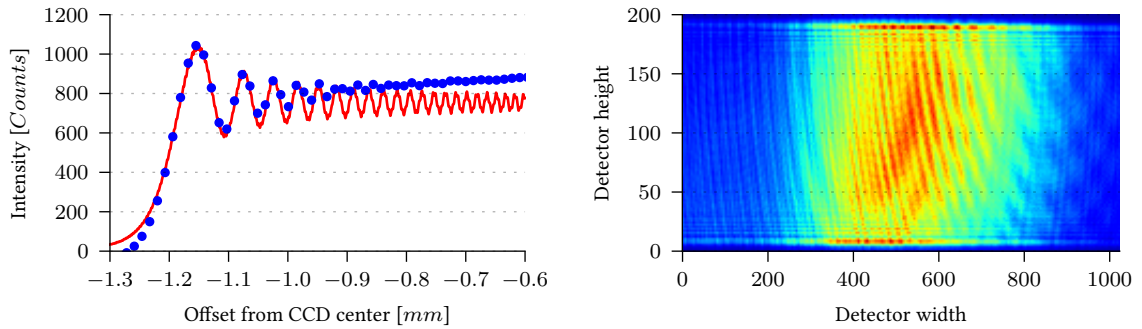


**Figure 2.13.: Measuring diffraction on a slit.** In order to characterize the diffraction by the slit, the CCD detector was placed as close as possible. The parameters were measured using a ruler and yielded distance  $d = (10.9 \pm 0.5)$  mm, opening  $a = (2.5 \pm 0.5)$  mm. The wavelength was  $\lambda = 852$  nm found from the laser specifications. The blue curve is the experimental data, while the red curve was fitted, leaving the distance and opening as free fitting parameters. They were found to be  $d' = (11.0 \pm 0.3)$  mm and  $a' = (2.470 \pm 0.013)$  mm, which is in close agreement with the measured values. The residual deviation in the amplitude are caused by Gaussian intensity distribution of the laser beam used for illumination.

The experimental diffraction pattern matches the theory very well, since the deviations are in the expected regimes. The function washes out as it approaches the centre of the chip. This is due to the nature of the pixels, which only have a finite size and the fact, that the frequencies of the oscillations are lower on the outer ends. All oscillations that fit into one pixel are averaged, therefore diffraction is not visible.

---

Why  
slit not  
in focus  
in 1:1?

### 2.4.3. Optimization of the masking setup

An important issue in the optimal placement of the slit is the distance from the CCD detector at which it is going to be placed. The frequency of the diffraction pattern depends on the distance  $d$ ; it is larger for smaller  $d$ , and smaller for larger  $d$ . In the limit  $\frac{a^2}{d\lambda} \ll 1$  the diffraction pattern of a point source is recovered (Fraunhofer diffraction in the far field).

This dependence on the distance was also tested experimentally and the results are shown in Figure 2.14. The optimal slit position is therefore close to the chip, since at this position the frequencies are maximal, therefore more oscillations fit into one pixel.

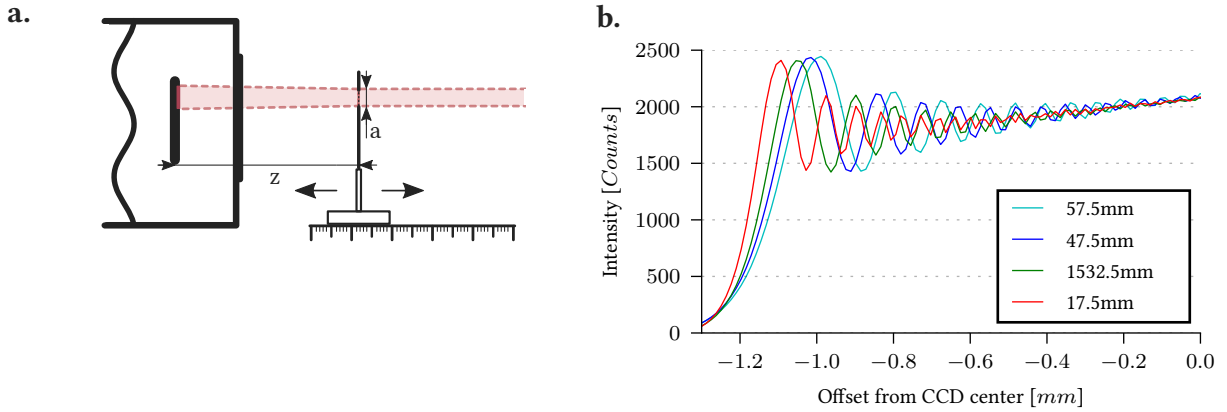


Figure 2.14.: **Distance dependent diffraction.** **a.** A slit was placed on a movable platform and diffraction was measured for various offsets  $z$ , while the slit opening  $a$  was kept constant. **b.** The diffraction frequency rises as the distance gets closer to the CCD.



## 3. Testing the camera: Superfluids

The purpose of the camera is to measure scientifically important data from dense atomic clouds consisting of Lithium and Caesium. The improvement of the resolution in the whole imaging setup now allows to find new attributes that could not be measured before and as an example, fermionic superfluids were chosen. The key signature of a superfluid transition can be found by creating a population imbalance, that then shows a unique structure in the centre of the cloud, differing them from the Thomas-Fermi distribution that is apparent in Bose-Einstein condensates (BEC).

### 3.0.1. Absorption imaging

In order to find microscopic attributes of atoms, or systems of atoms, it is necessary to look at the atoms themselves. This is commonly accomplished using either fluorescence or absorption imaging. In both cases, a laser beam is pointed at an atomic cloud, that is cooled and confined in a trap. In fluorescence imaging, the scattered light is collected, typically in a direction that is different than the illuminating beam. The intensity from the light through this method is not very high, since it is radiated in all directions. Therefore, long exposure times are required during which atoms can move and the information about the initial density and energy distribution is lost. Nevertheless, it is useful for single- and few-atom detection.

In contrast, in absorption imaging, the transmitted intensity of the imaging beam is recorded. Without atoms, one would see a beam profile of the laser. With atoms, a shadow is visible due to the atoms blocking the light. This is accomplished, by correctly tuning the laser to a resonance frequency of the atoms, which enables them to absorb the light, exciting them to a higher state. Through spontaneous emission, the atoms will decay, making it possible to excite them once again. This method works well, when the signal from the absorbed light is significantly larger compared to the noise sources.

better  
title

cite  
stephan  
helm-  
rich

cite si-  
mon  
mur-  
mann

cite phd  
thesis  
of Ser-  
wane,  
Selim,  
Science  
332, 336  
(2011)

still not  
sure  
about  
this...

There are a set of optical elements in the imaging path, like lenses to collimate the image and refocus it, or mirrors to guide the light into the camera. Since the surfaces will most likely introduce errors into the imaging, for example from impurities or dust, only the absorption image will not suffice to gain reliable data. This is compensated by taking a total of three pictures, in order to extract only the relevant information from the image.

This can be understood when looking at the light intensity  $I_{CCD}$  reaching the camera. The atom cloud has an optical density  $OD$ , therefore the intensity can be written as

$$I_{CCD} = I_0 e^{-OD} + I_{back}, \quad (3.1)$$

where it decreases from the incident laser intensity  $I_0$  due to light scattering by atoms. The intensity  $I_{back}$  describes the background signal, that is found when the CCD is not being illuminated by a laser such as readout noise, dark noise or stray photon light. All the interesting attributes of atoms are found by looking at the optical density, therefore in order to extract that, a background frame is subtracted from the absorption image and the laser profile divided, leaving

$$\frac{I_{CCD} - I_{back}}{I_0} = e^{-OD}. \quad (3.2)$$

The laser intensity  $I_0$  is measured in a separate frame, containing the laser intensity  $I'_0 = I_0 + I_{back}$  and also the background  $I_{back}$ . Finally, the equation yields

$$\frac{I_{CCD} - I_{back}}{I'_0 - I_{back}} = e^{-OD}. \quad (3.3)$$

From the resulting optical density, one can now conclude, for example, atom density distributions, atom numbers or excitation rates.

### 3.1. Previous observations in a polarized fermi gas

Superfluidity can be observed macroscopically for example in cooled Helium. As the fluid climbs walls and ignores its surface tension, it behaves in ways that are unintuitive at first. This is still mysterious in parts, therefore in order to understand superfluids better, an ultracold quantum system can be used as a model.

The first confident detection was carried out by M. Zwierlein et al in 2005. [A Bose-Einstein](#)

three  
images  
as ex-  
ample

read  
com-  
ment

cite  
zwier-  
lein see  
com-  
ment

condensate was prepared using evaporative cooling and a dipole trap. An additional laser beam, that is split using an acousto-optic deflector into two beams, that are separated by 3/4th of the trap diameter will then be used to "stir" the Lithium spin mixture.

This laser is merely used to prove, that a superfluid has been prepared. Upon rotation, when the correct feshbach resonances are applied, the condensate will start to create a vortex lattice, that is visible in the cloud as holes. In an optimal setup, the group was able to find up to 40 vortices in a single atomic cloud.

This laid the ground stone for the detection of superfluids, as no other effect is known to cause these vortices. Since it was possible from then on to prepare superfluids confidently, future research concentrated on understanding this exotic aggregate state.

The group of G. Partridge found an interesting effect when creating a spin imbalance rather than having 50% of each spin in the Fermi gas. In order to do that, a BEC was prepared and feshbach resonances are applied. A polarization  $P$  is introduced as  $P = (N_1 - N_2) / (N_1 + N_2)$  where  $N_i$  corresponds to either spin-up  $|1\rangle$  or spin-down  $|2\rangle$ . For the polarization  $P = 0$ , the cloud is still a BEC, although for higher polarizations, the atomic distribution is such that there is an inner unpolarized core which is surrounded by the majority component.

cite  
par-  
tridge

This has been further observed in the BEC-BCS crossover by T. De Silva and E. Mueller . They were also able to observe this structure consisting of an unpolarized inner core and the remaining majority components outside. They were also able to motivate this theoretically and found a formula for the distribution of the fermions.

cite

M. Zwierlein et al. and W. Ketterle continued this research and found that superfluidity can be directly observed from density profiles, without the need to ramp the magnetic field, which had to be used before. Such an achievement makes the theoretical description easier, therefore this is a great success. They showed the density profiles for at the BEC and BCS side of the Feshbach resonance and directly on resonance. Furthermore, the polarization  $P$  was probed in order to find an optimal setup, which seemed to be the case for  $P \sim 70\%$ .

cite

## 3.2. Implementation in the setup

The preparation of a fermionic superfluid is well documented, for example in , such that it should be possible to implement a sequence in our current setup in order to achieve this phase transition. In principle, the atoms are prepared at first in a MOT, then further cooled using D1 cooling and loaded into the dipole trap. In this optical trap, the spin imbalance is

cite  
zwier-  
lein  
nature  
2006

D1?

created. The dipole trap can then be further ramped to cool the remaining atoms evaporatively. For the detection of the superfluid, a time of flight method should be used. The trap depth is in the order of  $1\text{ }\mu\text{K}$ .

—> now our own measurement.

## **4. Conclusion and outlook**

## A. Acquisition sequence

During absorption image, the Andor camera will take eight images, which consist of two absorption, two division and four background images (or if the user specifies to only image one species, that then is one absorption and division image and six background images).

As the camera is only interested in the rising edge of the signal, the trigger length is not really important. But the chip will be exposed for the duration of the exposure time, after which the laser should be turned off. The, in our case, 204 pixels are then shifted downwards, taking  $t_{vshift}$ , which can be calculated by multiplying the vertical shift speed with the pixel height. For the fastest shift speed, this would result in

$$t_{vshift} = 2 \mu\text{spx}^{-1} * 204 \text{ px} = 408 \mu\text{s}, \quad (\text{A.1})$$

for the slowest speed we find

$$t_{vshift} = 64 \mu\text{spx}^{-1} * 204 \text{ px} = 13.1 \text{ ms} \quad (\text{A.2})$$

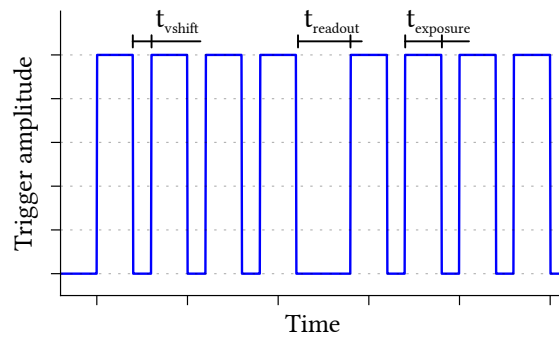


Figure A.1.: **Trigger signals.** The triggers are sent as a rectangular signal. The camera will interpret the rising edge of the signal as the starting point of the exposure. Here,  $t_{vshift}$  is the time it takes to shift the illuminated pixels downwards,  $t_{readout}$  is the time it takes the chip to read out the data and  $t_{exposure}$  the exposure time.

I'm not sure if this chapter belongs in the appendix. It is kind of a technical thing and I'm not sure where I could fit it in

Trigger number	Trigger time
1	0
2	$t_{trig}$
3	$2 * t_{trig}$
4	$3 * t_{trig}$
5	$4 * t_{trig} + t_{readout}$
6	$5 * t_{trig} + t_{readout}$
7	$6 * t_{trig} + t_{readout}$
8	$7 * t_{trig} + t_{readout}$

Table A.1.: **Trigger timing.** The trigger signals are limited by the readout speeds of the chip. This table lists the minimal timings necessary to fully read out the chip. Between signal 4 and 5, the illuminated pixels are still shifted downwards, before the chip is read out. This prevents introducing unnecessary errors, as all relevant pixels are then behind the cover of the slit.

Therefore the four subsequent signals can be taken after

$$t_{trig} = t_{vshift} + t_{exposure}. \quad (\text{A.3})$$

Four images are acquired until the readout process is started. This takes significantly longer, but as explained in Chapter 2.4.1 can be calculated via:

$$t_{ij} = i * v_{speed} + (i - 1) * j_{max} * h_{speed} + j * h_{speed}. \quad (\text{A.4})$$

For the whole chip, this gives us  $i = 4 * 204 = 816$ ,  $j = 1024$ ,  $j_{max} = 1024$ , therefore

$$t_{readout} = 816 * v_{speed} + 816 * 1024 * h_{speed}. \quad (\text{A.5})$$

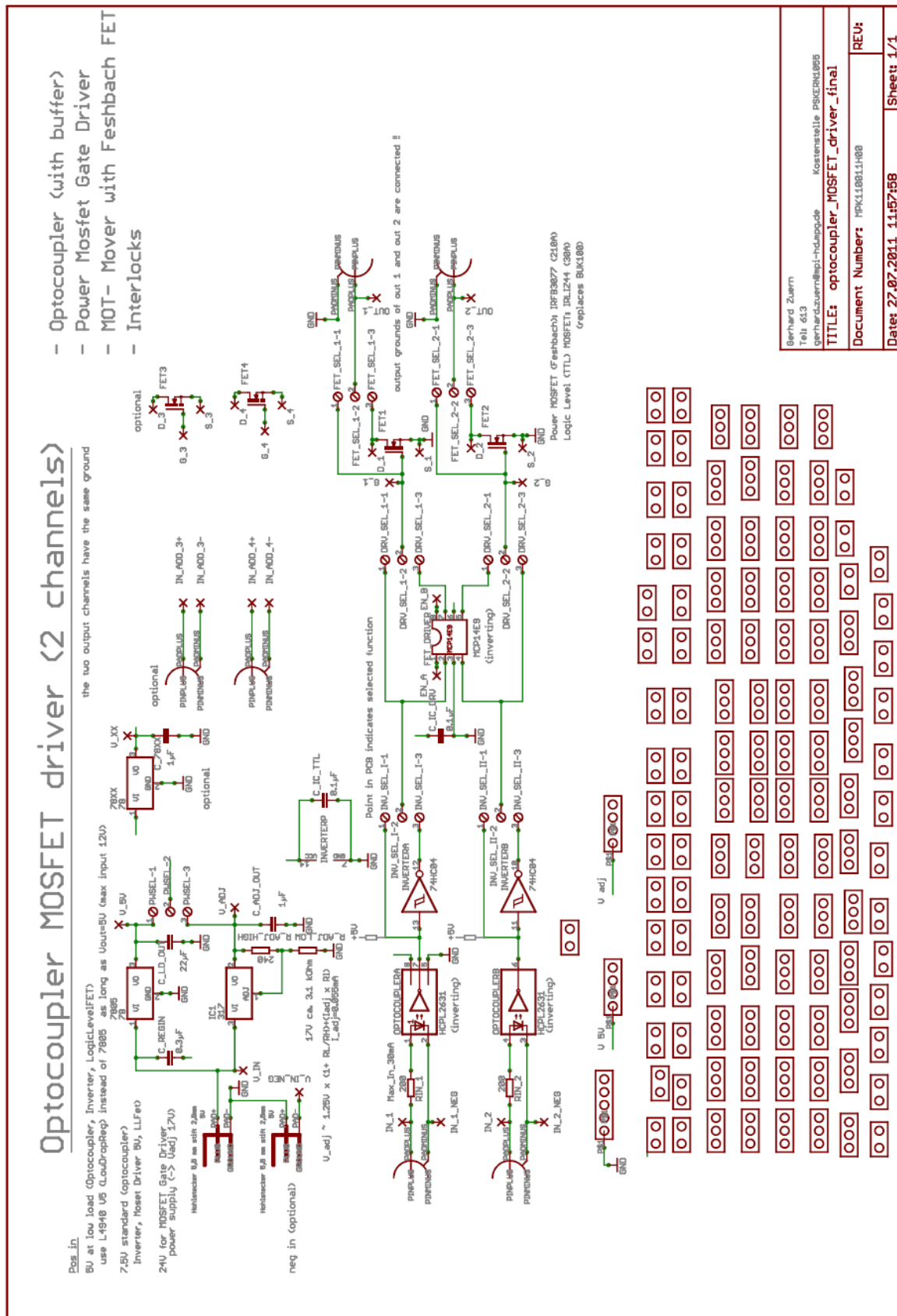
The trigger signals can finally be calculated via Table A.1.

## B. Shutter circuit

The circuit given on the next page is the complete circuit as opposed to Figure 2.6. The key difference here, is that the actual board contains two input/output ports and there are also converters (visible in the top-left corner), that keep the voltage at 24 V, which is necessary in order to use the MOSFET driver.

The breadboard on the bottom are built into the circuit, so that custom additions can be made, although this is not used in our case.





## C. Setup of the custom slit

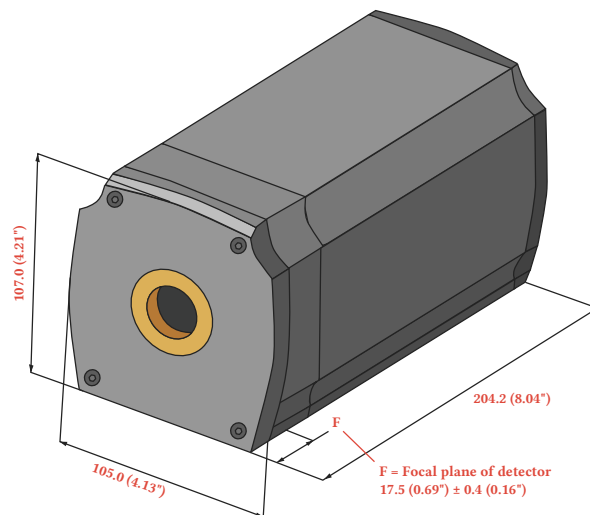


Figure C.1.: **Drawing of the camera.** As can be seen in this drawing, the CCD chip is first hidden behind a cover, that also includes an internal shutter and then offset by an additional 5 mm.

The cover, which can be seen in Figure ?? has a width of 12.5 mm, which adds additional space before the chip. The cover is mainly for a manual cap to cover the chip, when the camera is not used, and an internal shutter. Since we knew, that the internal shutter was not needed, we were able to remove the cover bringing us closer to the chip. Images of under the cover can be found in Appendix .

A/B/C?  
Image?

The holes for M4 screws were already there, so a custom plate was built on which the slit could be mounted on. In the technical drawing in Figure ??, the centre-most holes are reserved for the slit, which can be moved up and down to select the appropriate height needed for the imaging. The plate also gives the opportunity to move the whole set with the long holes in the outer-most edges.

It is also important to note, that the camera is very sensitive to stray light. The necessity to cover the laser path is unavoidable, but fortunately a simple solution. The plate offers

another set of screw holes, which will hold a SM2-mount, therefore eliminating any gap that could allow photons to reach the camera externally.

The long path of SM2 tubes then only allows the smallest amount of stray light to enter the camera, which will have significantly lower intensity than the actual absorption image.

# List of Figures

2.1. Imaging path . . . . .	2
2.2. Schematic design of a CCD array and its readout . . . . .	3
2.3. Shifting charges in a CCD detector . . . . .	4
2.4. Dark noise accumulation on the chip . . . . .	6
2.5. Readout noise . . . . .	7
2.6. Electronic circuit to control the shutter . . . . .	10
2.7. Probing the shutter for dynamics . . . . .	10
2.8. Shutter characterization . . . . .	11
2.9. Sample dynamics . . . . .	12
2.10. Shutter opening timings . . . . .	13
2.11. Schematics of imaging in the fast kinetics mode . . . . .	14
2.12. Diffraction on a single slit . . . . .	15
2.13. Measuring diffraction on a slit . . . . .	17
2.14. Distance dependent diffraction . . . . .	19
A.1. Trigger signals . . . . .	25
C.1. Drawing of the camera . . . . .	29

# Bibliography

- [1] Marc Repp. *Interspecies Feshbach Resonances in an Ultracold, Optically Trapped Bose-Fermi Mixture of Cesium and Lithium*. PhD thesis, Ruperto-Carola-University of Heidelberg, 2013.
- [2] Chris McFee. An introduction to ccd operation. [http://www.mssl.ucl.ac.uk/www\\_detector/ccdgroup/opttheory/ccdoperation.html](http://www.mssl.ucl.ac.uk/www_detector/ccdgroup/opttheory/ccdoperation.html). Accessed: 23 March 2016.
- [3] Allied Vision. Guppy f-038 datasheet.
- [4] M. Repp, R. Pires, J. Ulmanis, R. Heck, E. D. Kuhnle, M. Weidemüller, and E. Tiemann. Observation of interspecies  $^6\text{Li}$ - $^{133}\text{Cs}$  Feshbach resonances. *Phys. Rev. A*, 87:010701, Jan 2013.
- [5] Carmen Renner. Design and characterization of a dual-wavelength high-resolution imaging system. Master's thesis, University of Heidelberg, 2014.
- [6] Timo Bastian Ottenstein. A new objective for high resolution imaging of Bose-Einstein condensates. Master's thesis, University of Heidelberg, 2006.
- [7] *Skript zum Versuch F36 – Teil I "Wellenfrontanalyse mit einem Shack-Hartmann-Sensor" des Fortgeschrittenen-Praktikums II der Universitaet Heidelberg fuer Physiker*.
- [8] Simon Murmann. Toward the exact detection of mesoscopic atom numbers. Master's thesis, University of Heidelberg, 2011.
- [9] Daniel A. Steck. Quantum and atom optics. Available online at <http://steck.us/teaching>, April 2014. revision 0.9.10.